Journal of Solid State Chemistry 184 (2011) 797–804

Contents lists available at ScienceDirect

Journal of Solid State Chemistry

journal homepage: www.elsevier.com/locate/jssc

Palladium site ordering and the occurrence of superconductivity in $Bi_2Pd_3Se_{2-x}S_x$

R. Weihrich [a], S.F. Matar [b,*], I. Anusca [a], F. Pielnhofer [a], P. Peter [a], F. Bachhuber [a], V. Eyert [c]

[a] Institut für Anorganische Chemie, Universität Regensburg, Universitätsstraße 31, D-93040 Regensburg, Germany
[b] CNRS, University of Bordeaux, ICMCB, 87 avenue du Docteur A. Schweitzer, F-33600 Pessac, France
[c] Center for Electronic Correlations and Magnetism, Institute for Physics, University of Augsburg, D-86135 Augsburg, Germany

ARTICLE INFO

Article history:
Received 8 October 2010
Received in revised form
21 January 2011
Accepted 31 January 2011
Available online 1 March 2011

Keywords:
Parkerite
Superconductivity
DFT
Band structure
Chemical bonding

ABSTRACT

The crystallographic and electronic structures of compounds related to *parkerite* ($Bi_2Ni_3S_2$) are investigated with respect to the recently reported occurrence ($Bi_2Pd_3Se_2$) and absence ($Bi_2Pd_3S_2$) of superconductivity. Similarities and differences of the crystal structures are discussed within the series of solid solutions $Bi_2Pd_3S_{2-x}Se_x$ from powder and single crystal diffraction data. From crystal structure refinements, the question of different structures and settings of *parkerite* is discussed. Similar and different 2D and 3D partial Pd–*Ch* (*Ch*=S, Se) structures are related to half antiperovskite ordering schemes. To investigate the relation of low dimensional structures and the occurrence of superconductivity, electronic structures are analyzed by scalar-relativistic DFT calculations, including site projected DOS, ECOV and Fermi surfaces.

1. Introduction

Twenty years after the discovery of superconducting cuprates, novel pnictide superconductors like FeAsSmO or BaFeAs again initiated high interest in this field (see [1,2]). As both have layered crystal structures, attempts for a deeper understanding and design of superconductors based on structure–property relations [3–5] were encouraged. The crystal structures of cuprates like $YBa_2Cu_3O_{7-\delta}$ can be easily deduced from perovskites by an ordering scheme of unoccupied O sites [4]. Novel iron pnictides like FeAsSmO or BaFeAs form layered structures with sheets of $[FeAs]^-$. Relations of low dimensional crystal and electronic structures to superconductivity were recently shown for MgB_2 [6,7].

At that point, the recently discovered parkerite ($Bi_2Ni_3S_2$) type superconductors [8,9] become suitable to study structure–property relations. Their crystal structures were deduced as ordered half antiperovskites (HAP) $A_2M_3S_2=AM_{3/2}S$ [10,11] from the antiperovskite $MgNi_3C$ [12]. Within similar perovskite type $2\times2\times2$ supercells, differing ordering variants were found that determine the symmetry for $Pb_2Ni_3S_2$ (shandite, trigonal), $Bi_2Ni_3S_2$ (monoclinic) and $Bi_2Pd_3S_2$ (cubic). Ni–S layers are formed due to ordered occupation of half of the Ni sites within a $2\times2\times2$ superstructure in analogy to Cu–O sheets and partial O site occupation in cuprate superconductors. Related ordering schemes were found for trigonal $Pb_2Ni_3S_2=PbNi_{3/2}S$, cubic $Hg_3S_2Cl_2=Hg_{3/2}SCl$ and $K_2Pb_2O_3=KPbO_{3/2}$ (see [10,11]).

Superconductivity was observed for the isoelectronic parkerites $Bi_2Ni_3S_2$, $Bi_2Ni_3Se_2$ and $Bi_2Pd_3Se_2$, but not for $Bi_2Pd_3S_2$ [9]. Considering isotypic structures, this was surprising. From single crystal data, the Ni parkerites were shown to crystallize in monoclinic structures [13–15], but $Bi_2Pd_3S_2$ is cubic and isostructural (or isotypic) to $K_2Pb_2O_3$ [10,11]. Cubic and monoclinic parkerites were found to differ in terms of *M*=Ni, Pd site ordering and 2D versus 3D *M*–S substructures. Still a simple relation to the occurrence of superconductivity suffers from different settings given for $Bi_2Ni_3S_2$ and $Bi_2Ni_3Se_2$ by Brower et al. [15], Clauss et al. [16], Range et al. [13] and Baranov et al. [17]. All of these settings show complete *M*=Ni, Pd site ordering contrary to the first structure solution [18] that estimated partial disorder in an orthorhombic cell.

Thus, $Bi_2Pd_3Se_2$ served as a key compound to answer the question of how many different parkerite-type structures exist. No single crystal data were available and its structure could not be solved from powder diffraction [9]. Further, relations of the occurrence of superconductivity and *M* site ordering might help to understand electronic structure effects as estimated by the flat band/steep band concept [3].

In this paper, studies on possible structural changes within solid solutions $Bi_2Pd_3S_{2-x}Se_x$ are presented. The single crystal structures of $Bi_2Pd_3Se_2$ and $Bi_2Pd_3S_2$ are compared. Differences

* Corresponding author.
E-mail address: matar@icmcb-bordeaux.cnrs.fr (S.F. Matar).

0022-4596/$ - see front matter © 2011 Elsevier Inc. All rights reserved.
doi:10.1016/j.jssc.2011.01.037

in metrics, ordering and settings are discussed within the HAP model for $Bi_2Ni_3S_2$, $Bi_2Ni_3Se_2$, $Pb_2Pd_3Se_2$ and $Bi_2Pd_3S_2$. Thus, *M* site ordering determines structures and properties. Finally, DFT calculations are presented on the electronic structure and bonding of $Bi_2Pd_3Se_2$ that complement our earlier calculations [10,11].

2. Methods

2.1. Experimental methods

The samples were prepared from the elements in annealed quartz ampules by high temperature synthesis, as described

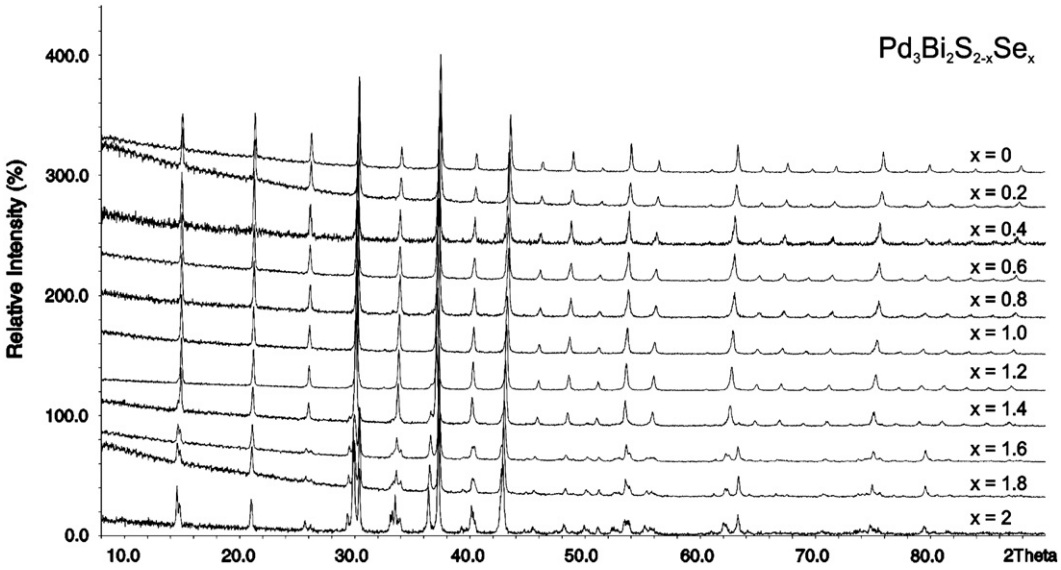

Fig. 1. X-ray powder diffraction for mixed crystals $Bi_2Pd_3S_{2-x}Se_x$.

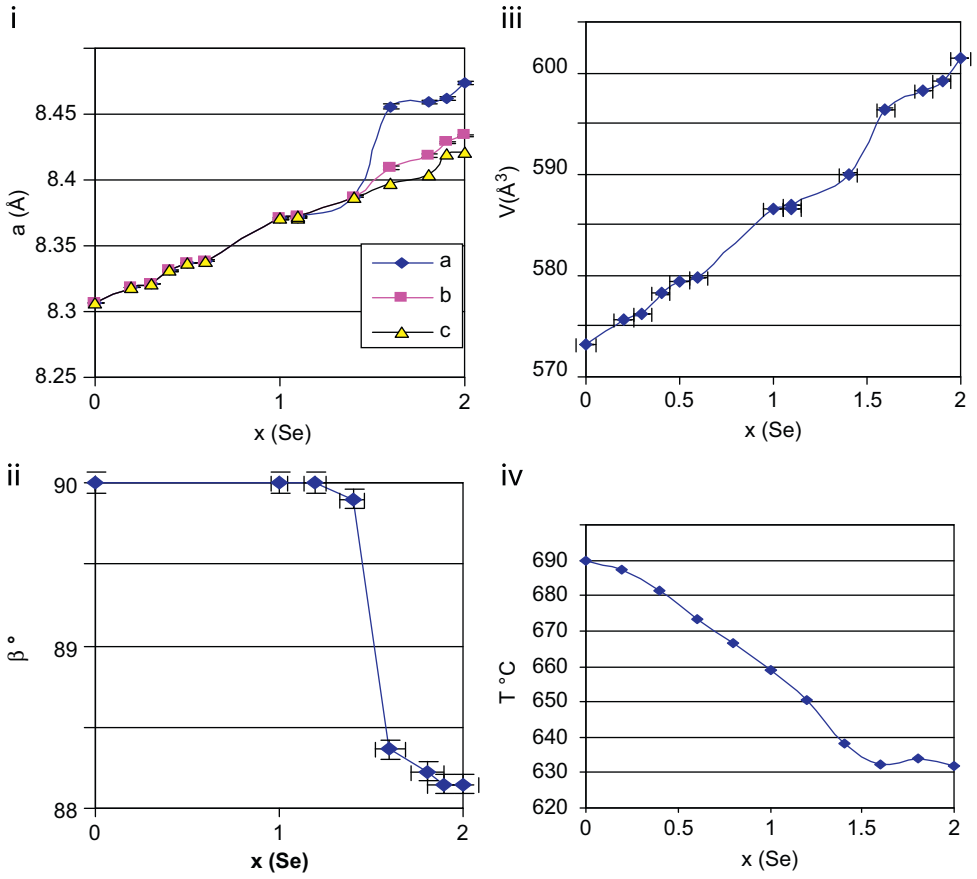

Fig. 2. $Bi_2Pd_3S_{2-x}Se_x$—determined lattice cell parameters *a, b, c* (*i*), monoclinic angle *β* (*ii*), volume (*iii*) and melting points (*iv*).

in [10,11]. After heating to 700 °C for one day, the temperature was decreased to 50° below the melting points for 2 days. X-ray experiments were carried out on Stoe diffractometers for powders (STADIP, Cu-$K\alpha$ radiation) and single crystals (IPDS, Mo-$K\alpha$). Data analysis and refinements were done with the codes WinXPow and SHELXL, as described in [19]. Melting points were determined by differential thermal analysis (DTA, Setaram TMA 92).

2.2. Computational details

As in our former work on the chalcogenide systems [10], the electronic band structure calculations are based on the density functional theory (DFT) [20] with exchange-correlation effects accounted for by the local density approximation (LDA) [21]. Although the gradient functional GGA could also be used, we noticed that the description of electronic (and derived) properties results obtained from LDA and GGA differ only slightly. The calculations were performed using the scalar-relativistic full-potential augmented spherical wave (ASW) method [22,23], which is well suited for all kinds of calculations, including spin-restricted ones. Here, we do not include the structure optimization. In the ASW method, the wave function is expanded in atom-centered augmented spherical waves, which are Hankel functions and numerical solutions of Schrödinger's equation, respectively, outside and inside the so-called augmentation spheres. In order to optimize the basis set, additional augmented spherical waves were placed at carefully selected interstitial sites (IS). The choice of these sites as well as the augmentation radii were automatically determined using the sphere-geometry optimization algorithm [24]. Self-consistency was achieved by a highly efficient algorithm for the convergence acceleration [25]. Brillouin zone integrations were performed using the linear tetrahedron method with an increasing precision on the **k**-mesh within the irreducible wedge of Brillouin zone (735 irreducible **k**-points out of 2744) [26]. In the minimal ASW basis set, we chose the outermost shells to represent the valence states and the matrix elements were constructed using partial waves up to $l_{max}+1=2$, for all constituents entered as neutral species. The completeness of the valence basis set was checked for charge convergence meaning that charge residues are ≤ 0.1 for $l_{max}+1$. The self-consistent field calculations were run to a convergence of $\Delta Q=10^{-8}$ for the charge density [24] and to 10^{-8} eV for the total energy. We also calculated the electronic structure of the sulfide homologue to establish comparisons. Information on the nature of the chemical interaction can be accessed within the ASW method in terms of the overlap population (S_{ij}) or the Hamiltonian H_{ij} one between two constituents i and j. A combination of both, avoiding ambiguities, was proposed by Fähnle et al. [27] with the ECOV (covalence bond energy) criterion. From the ECOV plots, negative, positive and zero (unit-less) ECOV magnitudes point to bonding, anti-bonding and non-bonding interactions, respectively. In this work, we use the ECOV criterion to carry out a qualitative chemical bonding analysis.

3. X-ray diffraction results

Changes in crystal structures from $Bi_2Pd_3S_2$ to $Bi_2Pd_3Se_2$ are first analyzed from powder diffraction (Figs. 1 and 2). Stepwise substitution of S by Se shows two major results: first, the overall scheme of reflections is maintained. Thus, the principle structural concept remains for the entire range of x(Se) contents. Second, a discontinuity in structural changes is observed at x(Se)=1.4. For lower contents of Se, the diffraction patterns can be indexed applying I centered cubic cells with lattice parameters $a=8.31$ Å ($x=0$) to $a=8.38$ Å ($x=1.4$). The cell volume increases gradually according to *Vegard*'s law because of the larger atomic radii of Se compared to S atoms. For higher x(Se) contents, the splitting of reflections indicates a deviation from cubic to monoclinic structure with differing lattice parameters a, b, c (see Fig. 2i). For $Bi_2Pd_3Se_2$, the lattice parameters are $a=8.466(1)$ Å, $b=8.434(1)$ Å and larger $c=8.431(1)$ Å. Further, the angle between a and c axes drops from $\beta=90°$ to 88° (Fig. 2ii).

The results are understood from recent crystal structure determinations (Fig. 3, for details see [10,11,19]). Single crystal data for $Bi_2Pd_3Se_2$ was refined within the space group $C2/m$ (for details see [19]) with an $R1=2\%$ value that is the best reached for parkerites to date. Now, we can show that this is valid for both settings according to Brower et al. and Clauss et al., for monoclinic $Bi_2Ni_3Se_2$ and $Bi_2Ni_3S_2$ [14,15]. One can conclude that these settings describe the same structure and that the superconducting parkerites are isotypic with similar layered monoclinic 2D structures. We have further shown from single crystal data that the structure of non-superconducting $Bi_2Pd_3S_2$ differs from the monoclinic parkerite-type structure not only in metrics, but in symmetry. $Bi_2Pd_3S_2$ is cubic, space group $I2_13$ [10,11], with a 3D Pd–S substructure.

Differences and similarities of these structures can be related to Pd site ordering within similar supercells. This is summarized in Fig. 3 for $Bi_2Pd_3S_2$ and $Bi_2Pd_3Se_2$ as discussed from superstructure and group–subgroup-relations to an antiperovskite type $BiPd_3X$ structure [18]. As expected from the substitution data, the structures are closely related in terms of primitive CsCl type Bi*Ch* partial structures. In both, $Bi_2Pd_3S_2$ and $Bi_2Pd_3Se_2$, only half of the Bi_4Ch_2 sites are occupied by M=Pd. However, they differ in the

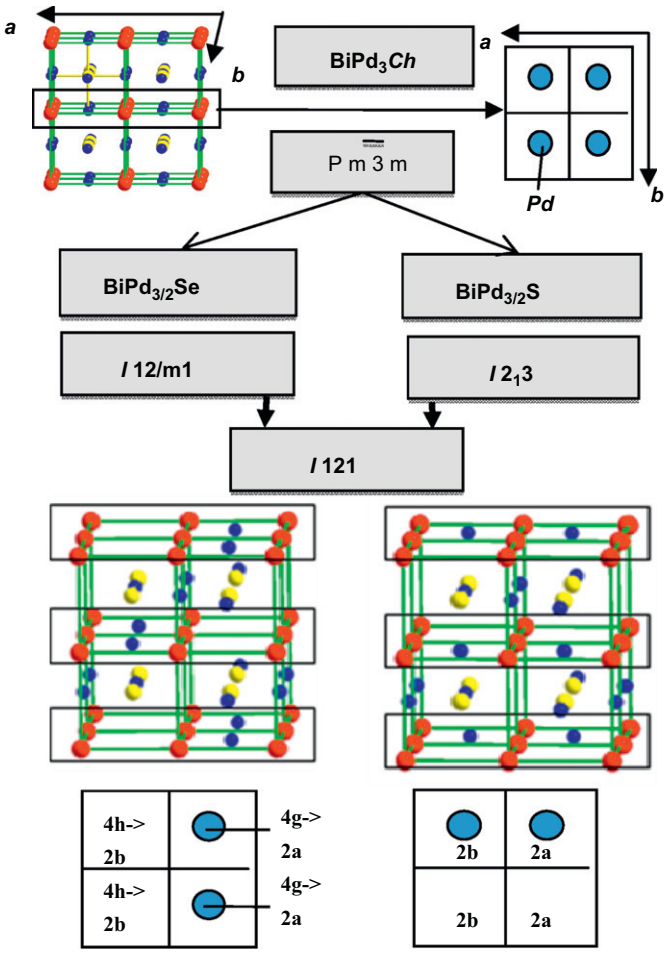

Fig. 3. Structure relations for perovskite type $BiPd_3C$, $BiPd_{3/2}Se$ and $BiPd_{3/2}S$.

occupation schemes. For both, chains of sharing polyhedra are formed within the faces of the Bi substructure separated by chains of unoccupied polyhedra. For the cubic structure, these chains run along different directions *x*, *y*, *z*, Pd atoms are equivalent by symmetry. A 3D Pd–S network is formed, the 3-fold symmetry axis is maintained.

For monoclinic $Bi_2Pd_3Se_2$, the layered structure is due to two chains of Pd occupied sites (4*g*, 4*f*) that run parallel within orthogonal faces of the Bi substructure. They define the monoclinic *b* axis along the "transition metal walls" in parkerites. From the *I* centered setting of the space group *C*2/*m* in Fig. 3, one can see that the occupation within the Bi superstructure faces of $Bi_2Pd_3Se_2$ is similar to $Bi_2Pd_3S_2$ within two faces, but it differs for one face (Fig. 3). For the face under discussion, Pd is found on 4*g* or 4*h* sites (equivalent by symmetry within the space group *C*2/*m*) in $Bi_2Pd_3Se_2$. The scheme found for $Bi_2Pd_3S_2$ can be represented in the space group *C*2 that is a common subgroup of $I2_13$ and *C*2/m. Refining both structures in space group *C*2, one finds the occupation of either two sites 2*a* or two sites 2*b* for $Bi_2Pd_3Se_2$ and one 2*a* and one 2*b* site $Bi_2Pd_3S_2$, as shown in Fig. 3. For the observations within the series $Bi_2Pd_3S_{2-x}Se_x$, a change in Pd site occupation has to be concluded at $x(Se)=1.4$. For lower Se contents, the structure is cubic, for higher it is monoclinic.

Finally the relation of occupation schemes and metrics is used to solve the question on different monoclinic parkerite-type structures and settings. Therefore, projections of Bi and *M* sites, as found for any monoclinic parkerite, are shown along the monoclinic *b* axis schematically in Fig. 4. The above discussed

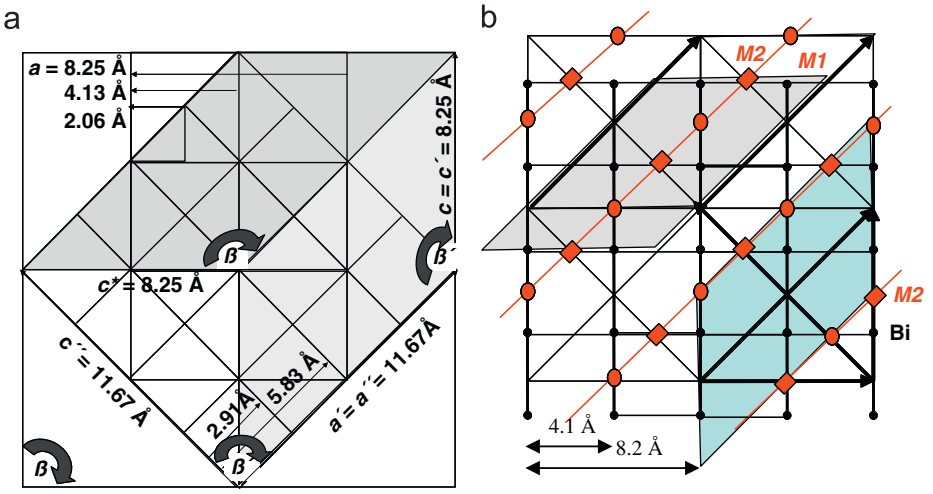

Fig. 4. (a, b) Metric relations for *a*, *c* axes, and *ß* angle for various settings in parkerites.

Table 1
Single crystal refinements on $Bi_2Pd_3Se_2$ and $Bi_2Pd_3S_2$ (supplementary data on single crystal structure determinations).

Formula sum	$Bi_2Pd_3Se_2$	$Bi_2Pd_3Se_2$
Setting	*Brower* [15]	*Clauss* [16]
Crystal system	monoclinic	monoclinic
Space group	*C*12/*m*1	*C*12/*m*1
Formula weight	3580.56	3580.56
Unit cell dimensions	$a=11.743(2)$ Å	$a=11.743(2)$ Å
	$b=8.431(2)$ Å	$b=8.431(2)$ Å
	$c=8.423(2)$ Å	$c=8.423(2)$ Å
	$\beta=133.93(1)^\circ$	$\beta=133.93(1)^\circ$
Cell volume	602.6(1) Å^3	602.6(1) Å^3
Density, calculated	9.903 g/cm^3	9.903 g/cm^3
Wyckoff sequence	ji^3hf	ij^3ge
Reflections	3040	3040
Unique Refl.	843	843
$R_{int}/R(\sigma)$	0.068/0.046	0.068/0.046
GooF	1.031	1.031
R1	0.029	0.029

Table 2
Comparison of lattice parameters for compounds $Bi_2M_3Ch_2$ (*Ch*=S, Se, *M*=Ni, Pd).

		a/Å	*b*/Å	*c*/Å	ß	*a*′/Å	ß′/°	*c*′/Å	ß″	*d*/Å	*d*′/Å
$Bi_2Pd_3S_2$	[10]	8.310	a	a	90	11.755	135	11.755	90	14.39	14.39
$Bi_2Pd_3Se_2$	This work	8.459	8.431	8.422	88.15	11.743	133.59	12.128	90.25	14.46	14.77
$Bi_2Ni_3S_2$	[15]	7.965	8.085	7.965	88.0	11.066	134.0	11.459	90.00		
$Bi_2Ni_3S_2$	[16]	7.960	8.078	7.963	88.0	11.066	134.0	11.451	90.01	13.70	14.01
$Bi_2Ni_3Se_2$	[17]	8.187	8.188	8.100	87.12	11.224	133.24	11.802	90.61	12.16	13.89

lattice parameters correspond to *I* centered parkerite type cells with β close to 90° as used by Range et al. [13]. Here, the supercell axis $a_I = c_I = 8.26$ Å of the monoclinic *I* centered cell is chosen arbitrarily. The standard *C* centered setting as used by Brower et al. and Clauss et al. [15,16] (Table 1) is found when a face diagonal of the *I* centered cell serves as monoclinic axis *a*′.

Table 3a
Atomic sites "fhi-I" and "fhi-II" (Clauss type) setting.

		$BiPd_{3/2}Se$	fhi-I		$BiPd_{3/2}Se$	fhi-II		$BiNi_{3/2}Se$		
Atom	***Wyck***	*x*	*y*	*z*	*x*	*y*	*z*	*x*	*y*	*z*
*Bi*1	4*i* (*m*)	0.2814	0	0.2972	0.2499	0	0.2586	0.2509	0	0.2569
*Bi*2	4*i*	0.2500	0	0.7412	0.2186	0	0.7027	0.2177	0	0.7020
*Pd*1	4*i*				0.0265	0	0.8015	0.0180	0	0.7904
	4*i*	0.0265	1/2	0.8017						
*Pd*2	4*h* (2)	0	0.2231	1/2	0	0.2768	1/2	0	0.2737	1/2
	4*g* (2)									
*Pd*3	4*f* (−1)	1/4	1/4	1/2	1/4	1/4	1/2	1/4	1/4	1/2
	4*e* (−1)									
*Se*7	8*j*	0.0336	0.2094	0.8217	0.0338	0.2903	0.8219	0.027	0.283	0.810

Table 3b
Atomic sites, "egi-I" (*brower* type) and "egi-II" setting.

		$BiNi_{3/2}S$			$BiPd_{3/2}Se$	egi-I		$BiPd_{3/2}Se$	egi-II	
Atom	***Wyck***	***x***	***y***	***z***	***x***	***y***	***z***	***x***	***y***	***z***
*Bi*1	4*i* (*m*)	0.25	0	0.25	0.2186	0	0.2028	0.2500	0	0.2413
*Bi*2	4*i*	0.25	0	0.75	0.24994	0	0.7586	0.2813	0	0.7972
*Pd*1	4*i*							0.0264	1/2	0.3014
	4*i*	0	0	0.25	0.0264	0	0.3014			
*Pd*2	4*h* (2.)									
	4*g* (2.)	0	0.25	0	0	0.2767	0	0	0.2233	0
*Pd*3	4*f* (-1)									
	4*e* (-1)	1/4	1/4	0	1/4	1/4	0	1/4	1/4	0
*Se*7	8*j*	0.07	0.25	0.265	0.0336	0.2094	0.8217	0.0338	0.2099	0.3219

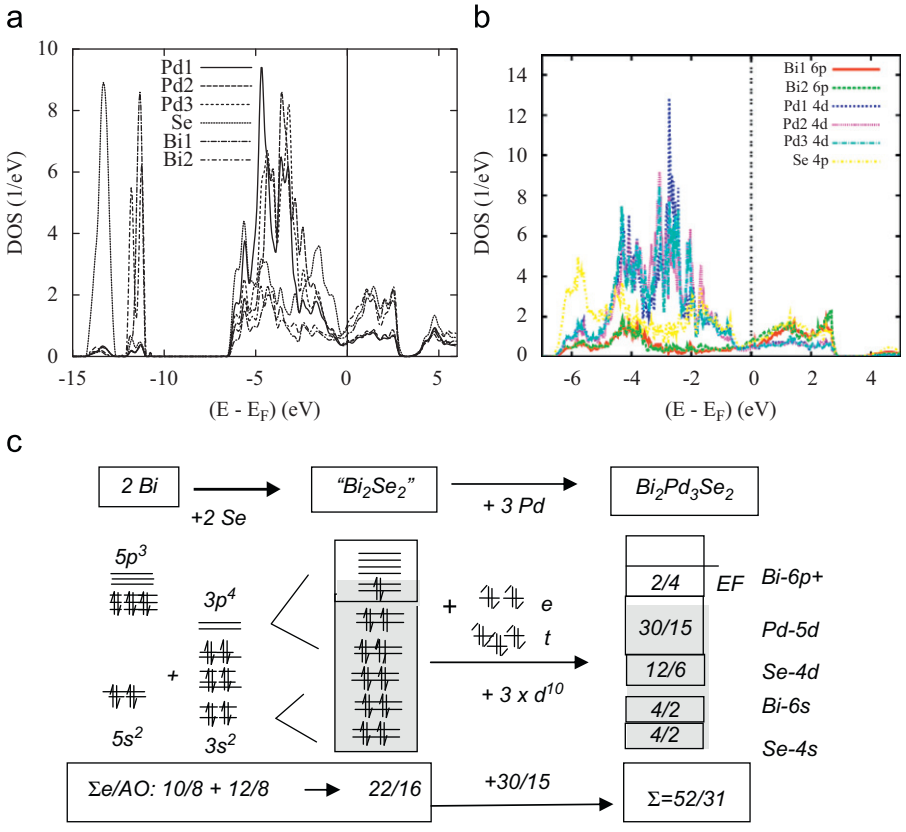

Fig. 5. $Bi_2Pd_3Se_2S$: its projected density of states accounting for site multiplicity for monoclinic $Bi_2Pd_3Se_2$ in a broad VB (a) and narrow VB (b) energy window. Sketch of atomic-molecular orbital diagram scheme in (c).

The angle ß′ is now close to 135°. Lastly Baranov et al. [17] chose a cell with both diagonals of the *I* centered cell as *a′* and *c′* axes with an angle ß′ again close to 90° (Table 2).

The respective lattice parameters are summarized for known compounds $Bi_2M_3Ch_2$ in Tables 3a and b. One can immediately see that $Bi_2Pd_3S_2$ serves as an exception with cubic metrics. This was the initial reason for our single crystal and DFT modeling studies [10,11]. All other *parkerite* related compounds show monoclinic distortions with ß=88° (*I* centering) or ß′ < 135° (*C*). Within the *I* setting the *b* axis is longer than a_I and c_I for *M*=Ni. As indicated in Fig. 4a, the problems of the settings concern the choice of the axes *a* and *c* and their origin. Little differing, long and short axis *a*, *c*, a_B' and c_B', as well as a possible shift of the origin along *a* and *c* is due to supercell structures. A reference for an undoubtable comparison is the *M*=Ni, Pd site occupation and ordering (Fig. 4 b). The shades in the monoclinic cells show shifts of the origin of *a* and *c* axes by 1/2. This is the simple difference of the settings of the cells due to Brower and Clauss [16]. The structures do not change by that. It explains also the occupation of the sites 4*i*, 4*g*, 4*e* as given for $Bi_2Ni_3S_2$ and 4*i*, 4*h*, 4*f* given for $Bi_2Ni_3Se_2$ [15]. The pairs of 4*i* sites (*m* symmetry), of 4*f* and 4*e*, as well as 4*h* and 4*g* are equivalent by symmetry. They are just shifted by 1/2 along *a*, *b*, or *c*.

One can conclude on the structures: all known superconducting parkerites show similar monoclinic layered structures. Seemingly differences are due to different settings well known within the space group *C*2/m. Non-superconducting $Bi_2Pd_3S_2$ is not monoclinic. It is cubic and it differs from the monoclinic parkerite in *M* site ordering. It is the *M* site occupation scheme that unambiguously determines the parkerite-type structure. The metric distortions and the layered structures of the monoclinic parkerites are consequences of this occupation scheme. Analogously to the structure, we expect similarities and differences in the electronic structures of $Bi_2Pd_3S_2$ and $Bi_2Pd_3Se_2$ that should be related to Pd site occupation and the occurence of superconductivity of the 2D structures that is absent for the 3D structure.

4. Electronic structure results

The electronic structure analysis should help to understand bonding and band changes at E_F that can have an effect on superconductivity of the monoclinic structure, complementary to our earlier analysis of the cubic structure of $Bi_2Pd_3S_2$ [10].

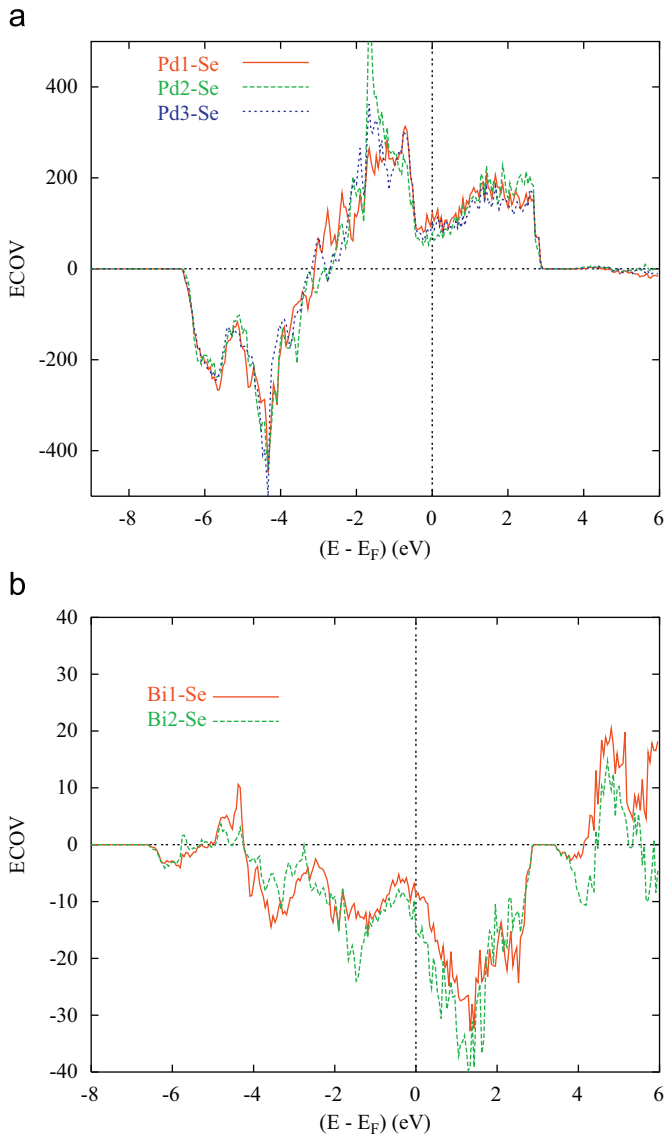

Fig. 6. Chemical bonding from ECOV unit-less criterion for pair interactions within $Bi_2Pd_3Se_2$: (a) Pd–Se and (b) Bi–Se.

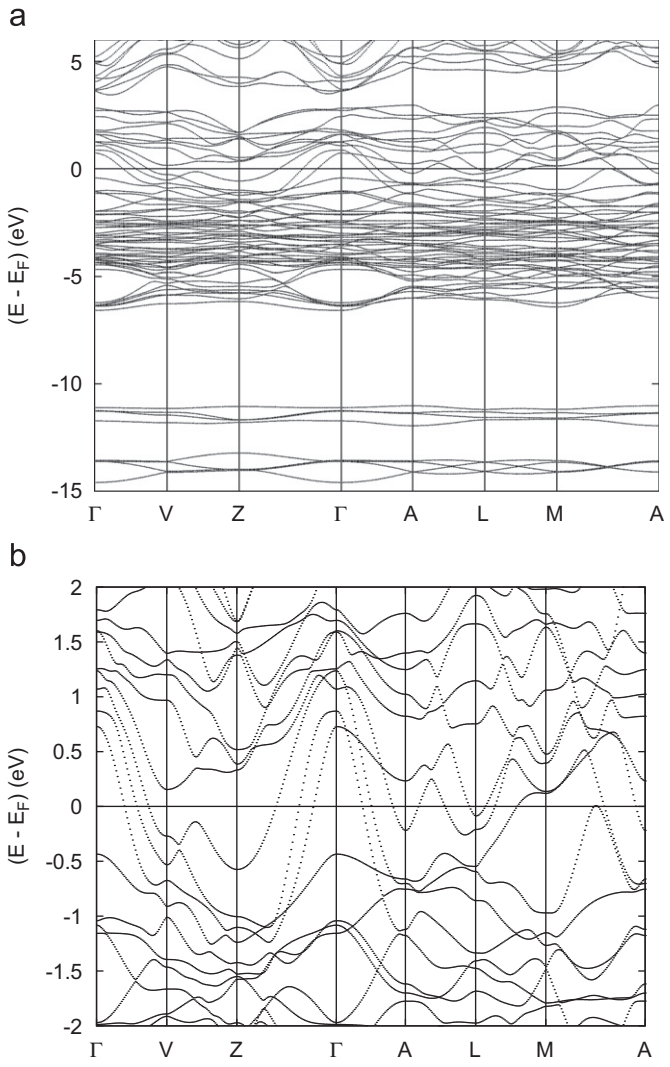

Fig. 7. $Bi_2Pd_3Se_2$: band structure along the major directions of the irreducible wedge of base-centered monoclinic Brillouin zone. (a) Broad energy window with the corresponding DOS and (b) narrow energy window showing the large band dispersion at E_F.

4.1. Site projected DOS

Fig. 5a shows the site projected DOS of the monoclinic $Bi_2Pd_3Se_2$. The valence band VB is dominated by a low energy region with *s* states of selenium at lower energy than Bi ones due to the difference of electronegativity between the two: $\chi Se = 2.55 > \chi Bi = 2.0$. Their *p* states extend over the higher part of the VB, where they mix with the Pd 4*d* states which are broadened over ~6 eV. This is due to their belonging to the 2nd transition metal series and to their mixing with the Se *p* states as detailed in the narrow energy PDOS shown in Fig. 5b. As palladium is a late element of the 4*d* series, the large filling of its *d* states up to ~8.4 electrons makes them centered well below the Fermi level (E_F). Then, E_F is crossed by low intensity itinerant like *s,p* like states arising from all constituents. In a band structure description, they will be signaled by a large dispersion band, i.e. contrary to flat localized bands characterizing *d* (and *f*) subshells (cf. Fig. 7a). We note here that same PDOS features are observed for the cubic system as well as for the sulphide, especially as concerns the itinerant DOS at E_F.

The DOS analysis can be summarized by the diagram sketched in Fig. 5c. From an ionic point of view, the "Bi_2Se_2" substructure of the parkerite has 22 valence electrons (VE): 20 VE fully occupy the Se-4*s*, Bi-6s and Se-4*p* orbitals, 2 VE are found in Bi-5*p* states. Estimating now fully occupied Pd-$4d^{10}$ orbitals (five Pd atoms $= 3 \times 10$ VE in $5 \times 3 = 15$ orbitals), this picture can be transferred to $Bi_2Pd_3Se_2$, i.e. the valence region is mainly due to Bi-6*p*. Indeed, the calculated DOS shows a gap close to E_F that separates Pd-4*d* and Bi-6*p*. The limitations of the simple ionic picture are seen from contributions of Pd-4*d* and Se-4*p* to the VB region that must be attributed to antibonding states from covalent Pd–Se- and Bi–Se interactions.

4.2. Analysis of the chemical bonding

These features are more detailed with the plot of pair interactions within two panels of ECOV plots shown in Fig. 6a and b for Pd–Se and Bi–Se, respectively. In the lower part of the VB few effects are observed, so that we limit the analysis to the upper part of the VB, in a narrow energy range around E_F. Fig. 6a shows that the bonding strength is nearly equivalent for all three Pd with Se. The lower energy half of the VB is bonding, while the other half extending to E_F and above is antibonding corresponding to π, π^*. This characterizes Pd bonding with the *4d* states which are nearly filled, so that extra electrons lead to antibonding states and the resulting Pd–Se interaction feature points to an overall antibonding behavior, especially exhibited at E_F. At E_F and above, σ^* antibonding states are assigned from their itinerant behavior. Then, the itinerant states at the Fermi level are partly due to antibonding Pd–Se. Turning to the other type of interactions, Bi–Se are bonding for both sub lattices of Bi as shown in Fig. 5b. This agrees with the crystal structure description with Bi_4Se_2 bipyramides. However, their overall intensity is ~10 times lower than Pd–Se ones, due to the different nature of the valence states involved: *s,p* versus *d* in the former. Nevertheless the feature of the presence of both bonding and antibonding chemical interactions at E_F is noteworthy.

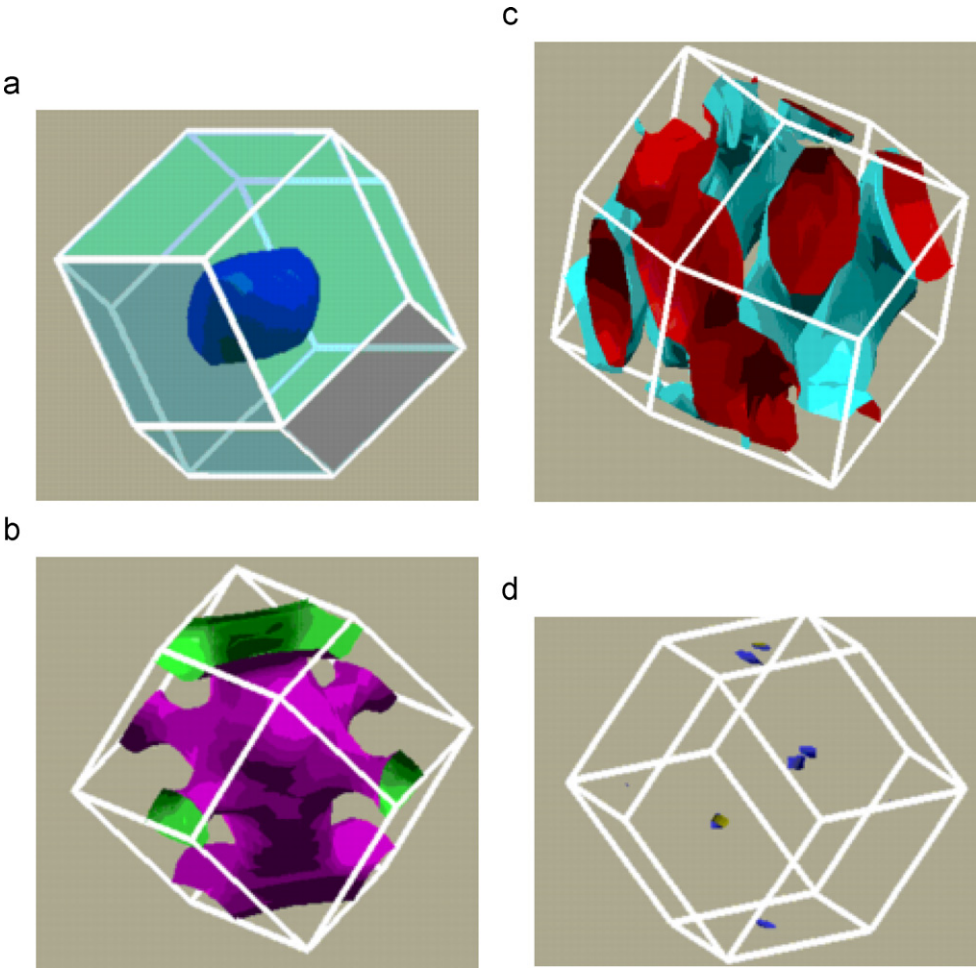

Fig. 8. $Bi_2Pd_3Se_2$: Fermi surfaces corresponding to the band structure in Fig. 7b.

4.3. Band structure

For the sake of detailing the nature of the bands along the main directions of the base-centered monoclinic Brillouin zone, we show in Fig. 7a and b the band structure of the whole energy range shown with the corresponding DOS of Fig. 5a, and over a small energy window around E_F.

From Fig. 7a, the isolated low energy lying in Se and Bi *s* states are found in the energy range {−15, −10 eV}, then the broad DOS due to Pd 4*d* is found in less dispersed band between −6 eV and E_F (cf. Fig. 5a). Around E_F the dispersive bands corresponding to the itinerant DOS are observed. Focusing on this energy region, Fig. 7b shows a smaller energy window around E_F, where essential features appear as to three bands along $\Gamma(0,0,0)-V(0,0,1/2)$ direction of the Brillouin zone (this is repeated in other directions ex. $Z(0\ 1/2\ 1/2)\ -\Gamma$) corresponding to hole carriers as well as to electron carriers ex. between $M(1/2\ 1/2\ 1/2)$ and $A(1/2\ 0\ 0)$; notice the dispersed band just lying at the Fermi level. Such a situation resembles that of the high T_C superconductor MgB_2 investigated by electron energy-loss spectroscopy and first-principles calculations [7,28], which exhibits (bi-dimensional) 2D and (tri-dimensional) 3D Fermi surfaces (FS). For $Bi_2Pd_3Se_2$, the corresponding FS are shown in Fig. 8. Although their assignment is rather complex, it is interesting to trace out a 2D-like FS in Fig. 8b, while the other show 3D-like features.

5. Concluding remarks

From X-ray diffraction data refinements, $Bi_2Pd_3Se_2$ was shown to be isopointal with parkerite, $Bi_2Ni_3S_2$ and $Bi_2Ni_3Se_2$. From the point of view of symmetry and an earlier presented occupation scheme, all superconducting parkerites show the same monoclinic layered structure. Within the series of solid solutions, $Bi_2Pd_3S_{2-x}Se_x$ discontinuities in metrics and melting points have to be attributed to a change in structure and symmetry from $x=1.4$ to 1.6. It is due to a difference in Pd site ordering that changes also the Pd–*Ch* network from 3D for *Ch*=S rich to 2D Se for Se rich compounds. Because of the similar local structures, coordination and bonding the differences are small. This is also seen for the electronic structure that was systematically deduced from substructures. Bonding and antibonding states of Bi-6p, Pd-4d and Se-4p contribute to the flat and steep bands at E_F that might be due to the concept of Simon [6]. From the point of view of symmetry, the absence of superconductivity in cubic $Bi_2Pd_3S_2$ might be seen as a hint that it is related to the layered structure analogously to cuprates and the novel oxopnictides. Hints are given from the Fermi surface that is isotropic contrary to 2D features found for monoclinic $Bi_2Pd_3Se_2$. Electronic structure effects related to the anisotropy in dynamics as driven by phonons and CDW might play an important role for parkerites and remain to be investigated.

Acknowledgments

Thanks are given to the group of F. Rau, Dr. M. Zabel and M. Andratschke from the group of Prof. A. Pfitzner for support in X-ray-measurments and data collection. The Deutsche Forschungsgemeinschaft (DFG) is acknowledged for financial support. This work was supported by the Deutsche Forschungsgemeinschaft through TRR 80. Computation facilities provided by the University of Bordeaux are gratefully acknowledged.

References

[1] J.G. Bednorz, K.A. Müller, Angew. Chem. 100 (1988) 757.
[2] D. Johrendt, R. Pöttgen, Angew. Chem. 120 (2008) 4860;
R. Pöttgen, Angew. Chem. Int. Ed. 47 (2008) 4782.
[3] A. Simon, Angew. Chem. 109 (1997) 1873;
A. Simon, Angew. Chem. Int. Ed. 36 (1997) 1788.
[4] H. Müller-Buschbaum, Angew. Chem. 101 (1989) 1503.
[5] M. Bäcker, A. Simon, R.K. Kremer, H.-J. Mattausch, R. Dronskowski, J. Rouxel, Angew. Chem. 108 (1996) 837;
H. Mattausch, A. Simon, C. Felser, R. Dronskowski, Angew. Chem. 108 (1996) 1805;
S. Deng, J. Köhler, A. Simon, Angew. Chem. 118 (2006) 613;
S. Deng, J. Köhler, A. Simon, Angew. Chem. Int. Ed. 45 (2006) 599.
[6] S. Deng, A. Simon, J. Köhler, A. Bussmann-Holder, J. Supercond. 16 (2003) 919.
[7] C. Ma, R.J. Xiao, H.X. Geng, H.X. Yang, H.F. Tian, G.C. Che, J.Q. Li, Ultramicroscopy 108 (2008) 320.
[8] T. Sakamoto, M. Wakeshima, Y. Hinatsu, J. Phys., Condens. Matter 18 (2006) 4417.
[9] T. Sakamoto, M. Wakeshima, Y. Hinatsu, K. Matsuhira, Phys. Rev. B 78 (2008) 024509.
[10] R. Weihrich, S.F. Matar, V. Eyert, F. Rau, M. Zabel, M. Andratschke, I. Anusca, Th. Bernert, Prog. Solid State Chem. 35 (2007) 309.
[11] R. Weihrich, I. Anusca, Z. Anorg. Allg. Chem. 632 (2006) 335.
[12] T. He, Q. Huang, A.P. Ramirez, Y. Wang, K.A. Regan, N. Rogado, M.A. Hayward, M.K. Haas, J.S. Slusky, K. Inumara, H.W. Zandbergen, N.P. Ong, R.J. Cava, Nature 411 (2001) 54.
[13] K.-J. Range, M. Zabel, S. Wandinger, H.P. Bortner, Rev. Chim. Miner. 20 (1983) 698.
[14] D.L. Scholtz, Trans. Geol. Soc. S. Afr. 39 (1937) 81–210.
[15] W.S. Brower, H.S. Parker, R.S. Roth, Am. Mineral. 59 (1974) 296.
[16] A. Clauss, K. Weber, Neues Jahrb. Mineral., Monatsh. 385 (1975) 95;
A. Clauss, Naturwissenschaften 64 (1977) 145.
[17] A.I. Baranov, A.V. Olenev, B.A. Popovkin, Russ. Chem. Bull. 50 (2001) 353.
[18] M.E. Fleet, Am. Mineral. 58 (1973) 435.
[19] S. Seidlmayer, F. Bachhuber, I. Anusca, J. Rothballer, M. Bräu, P. Peter, R. Weihrich, Z. Krist. 225 (2010) 371.
[20] P. Hohenberg, W. Kohn, Phys. Rev. B 136 (1964) 864;
W. Kohn, L.J. Sham, Phys. Rev. A 140 (1965) 1133.
[21] S.H. Vosko, L. Wilk, M. Nusair, Can. J. Phys. 58 (1980) 1200.
[22] A.R. Williams, J. Kübler, C.D. Gelatt, Phys. Rev. B 19 (1979) 6094.
[23] V. Eyert, The Augmented Spherical Wave Method—A Comprehensive Treatment, Lecture Notes in Physics, Springer, Heidelberg, 2007.
[24] V. Eyert, K.H. Höck, Phys. Rev. B 57 (1998) 12727.
[25] V. Eyert, J. Comput. Phys. 124 (1996) 271.
[26] P.E. Blöchl, Phys. Rev. B 50 (1994) 17953.
[27] G. Bester, M. Fähnle, J. Phys.: Condens. Matter 13 (2001) 11541.
[28] S.F. Matar, Z. Naturforsch. 63b (2008) 673.